Journal of Biomedical Optics 7(3), 478–485 (July 2002)

Photon pathlength determination based on spatially resolved diffuse reflectance

Henrik Nilsson
Marcus Larsson
Gert E. Nilsson
Tomas Strömberg
Linköpings universitet
Department of Biomedical Engineering
University Hospital
S-581 85 Linköping, Sweden

Abstract. A method for the prediction of the average photon pathlength in turbid media has been developed. The method is based on spatially resolved diffuse reflectance with discrete source detector distances up to 2 mm. Light reflectance was simulated using a Monte Carlo technique with a one-layer model utilizing a wide range of optical properties, relevant to human skin. At a source detector separation of 2 mm, the pathlength can vary sixfold due to differences in optical properties. By applying various preprocessing and prediction techniques, the pathlength can be predicted with a root-mean-square error of approximately 5%. Estimation of the photon pathlength can be used, e.g., to remove the influence of optical properties on laser Doppler flowmetry perfusion readings, which are almost linearly related to the average photon pathlength. [DOI: 10.1117/1.1482378]

Keywords: tissue optical properties; diffuse reflectance; Monte Carlo simulations; laser Doppler flowmetry; photon pathlength.

Paper JBO-01044 received June 29, 2001; revised manuscript received Dec. 12, 2001; accepted for publication Jan. 14, 2002.

1 Introduction

Photon migration through a turbid medium, e.g. tissue, depends on the optical properties of that medium. These properties are represented by the absorption (μ_a) and scattering (μ_s) coefficients, the probability distribution of the scattering angles, $p(\theta)$, and the tissue refractive index. Recently, large efforts have been spent on *in vivo* determination of the tissue optical properties, using affordable techniques, such as measurement of the spatially resolved diffuse reflectance, that can be implemented in instruments for clinical use.[1–9] The optical properties can be used directly for diagnostics, since, e.g., brain and breast tumors have higher absorption than surrounding, non-neoplastic tissue.[1,10] Furthermore, knowledge of tissue bulk absorption at distinct wavelengths can be used for analysis of the tissue content of major chromophores, such as hemoglobin, melanin, fat, and water.[10]

By using two wavelengths, the relative amounts of oxygenated and reduced hemoglobin can be estimated, as in pulse oximetry. However, the latter method is based on the assumption that the migrated photon pathlength is equivalent at the two different wavelengths[6]—an assumption that can be questioned, considering the fact that optical properties display a wavelength dependence.[9,11] Laser Doppler flowmetry (LDF) is an established method for monitoring microvascular perfusion *in vivo*. However, one problem with the method is the difficulty in making inter- and even intraindividual comparisons, due to varying tissue optical properties. It has been shown, that for a constant perfusion, the LDF output signal is affected both by changes in scattering and absorption of the turbid medium.[12] The generated perfusion estimate is based on the interaction between photons and moving scatterers, an estimate sensitive to both the velocity and concentration[13] of moving scatterers (mainly red blood cells) as well as the photon pathlength.[14,15] The origin of the pathlength variations is not only found in the tissue optical properties, but also in the source detector separation, ρ, of the LDF probe (normally 0.25–1 mm).[12,15]

The tight relationship between optical properties and photon pathlength suggests that similar approaches could be used in estimating the two; hence, possibly enabling us to eliminate the pathlength influence on the LDF readings. To our knowledge, no author has previously presented a method based on local reflectance at small ρ for determination of the photon pathlength in a turbid medium. Such a method could also be used for further development of pathlength dependent methods, e.g. pulse oximetry and reflectance spectroscopy. Therefore, the aim of the present study is to develop a method for local estimation of photon pathlength, using the spatially resolved diffuse reflectance profile in the 0–2 mm range.

We will show in this paper, that for a wide range of optical properties, applicable to human skin, the average pathlength can vary by almost a factor 6 for a source detector separation of 2 mm. We have devised methods based on a one-layer homogenous tissue model, that can predict the average pathlength of the photons at various source detector separations, with a root-mean-square (rms) error of about 5%.

2 Materials and Methods

2.1 Simulation Model

For small source detector separations (0–2 mm) and optical properties where $\rho\mu_s' < 10$ [$\mu_s' = \mu_s(1-\langle\cos\theta\rangle)$, the reduced scattering coefficient, $\langle\cos\theta\rangle$=average cosine of the scattering angles], the diffusion approximation of the transport equation is not generally applicable.[2,16] Further, the diffusion ap-

Address all correspondence to Henrik Nilsson. Tel.: +46-13-222000; Fax: +46-13-101902; E-mail: henni@imt.liu.se

1083-3668/2002/$15.00 © 2002 SPIE

Table 1 Optical properties of the reference space. $\langle\cos\theta\rangle$: mean cosine of the photon scattering angle, θ, calculated from the combination of 96% Henyey–Greenstein phase function, and 4% isotropic scattering.

μ_a (mm^{-1})	0.01	0.05	0.10	0.15	0.20	0.25
μ_s (mm^{-1})	5	10	20	30	40	50
$\langle\cos\theta\rangle$	0.80	0.85	0.90	0.95		

proximation is only valid when $\mu_s' \gg \mu_a$.[16,17] Therefore, with the setup used in the present study, photon pathlengths must be statistically determined by means of Monte Carlo simulations. The Monte Carlo simulation software used in this study was developed by de Mul et al. (MontCarl 2001, version 20.01 a).[18]

For all simulations, a homogenous semi-infinite slab with a thickness of 100 mm with different optical properties according to Tables 1 and 2, was used. A low concentration of homogeneously distributed moving scatterers (corresponding to $\mu_s = 0.1$ mm^{-1}) with a constant velocity, $v = 1.0$ mm/s, parallel to the slab surface, was introduced in the model. All scattering events, due to both moving and static scatterers, were modeled with the same phase function. In order to estimate the LDF perfusion, all Doppler shifts due to photon interactions with moving scatterers were stored. The refractive index of the ambient air was set to $n = 1.0$, whereas the refractive index of the slab was set to $n = 1.44$, which is considered a relevant value for human skin.[19,20] A divergent circular light beam (NA = 0.37) with a diameter of 0.2 mm and a rectangular intensity distribution impinged on the slab surface. All photons exiting the upper slab surface at a radial distance (ρ) from the center of the source in the range $0.13 \leqslant \rho \leqslant 2.17$ mm were detected. This geometry was subsequently transformed mathematically into mimicking a linear array of ten fibers, with one transmitting, and nine receiving fibers (Figure 1). The fibers were located adjacent to each other, with a center-to-center separation of 230 μm, each fiber having a core diameter of 200 μm, and a surrounding cladding with a thickness of 15 μm. The specific geometrical and optical properties of the simulated fiber optic probe is similar to a probe we have previously used for LDF measurements.[12] In all simulations, 500 000 photons were detected. The number of emitted photons in each simulation ranged from less than 800 000 to more than 16 million for the different setups of optical properties. In order to simulate a light source with a constant intensity, the number of detected photons was normalized by the number of emitted photons.

Table 2 Optical properties of the validation space. $\langle\cos\theta\rangle$: mean cosine of the photon scattering angle, θ, calculated from the combination of 96% Henyey–Greenstein phase function, and 4% isotropic scattering.

μ_a (mm^{-1})	0.03	0.075	0.125	0.175	0.225
μ_s (mm^{-1})	7.5	15	25	35	45
$\langle\cos\theta\rangle$	0.825	0.875	0.925		

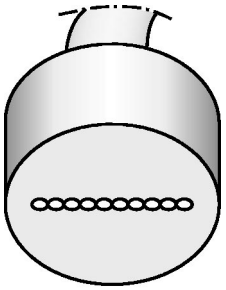

Fig. 1 Probe design. Ten fibers are arranged in a linear array, and each fiber has a core diameter of 0.2 mm (0.23 mm including cladding).

The Henyey–Greenstein phase function[21]

$$p_{\mathrm{HG}}(\theta) = \frac{1}{4\pi}\,\frac{1-g_{\mathrm{HG}}^2}{(1+g_{\mathrm{HG}}^2-2g_{\mathrm{HG}}\cos\theta)^{3/2}} \qquad (1)$$

was used in conjunction with an isotropic phase function to describe the photon scattering, where θ is the deflection angle and g_{HG} is the anisotropy factor. The proportions used were 96% Henyey–Greenstein and 4% isotropic phase function. Hence, the resulting phase function can be expressed as

$$p(\theta) = \frac{\beta}{4\pi} + (1-\beta)p_{\mathrm{HG}}(\theta), \qquad (2)$$

where $\beta = 0.04$. This combination of a highly forward scattering component, such as the Henyey–Greenstein phase function ($g_{\mathrm{HG}} \geqslant 0.7$), and an isotropic component, has been found to adequately describe light scattering in biological tissues.[1,2]

A large reference space, used to develop pathlength estimation methods, was defined. It consisted of equidistant optical properties, with the intention to encompass the range of values from *in vitro* and *in vivo* estimations of human epidermis and dermis at $\lambda = 632$ nm.[11,19,20,22] Therefore, all combinations of parameters in Table 1 were chosen as input parameters in the Monte Carlo model, thus, requiring $6 \times 6 \times 4 = 144$ simulations.

Second, a validation space for evaluation of the accuracy of the pathlength estimation methods was defined. It was setup to maximize the distances to the nearest combination of optical properties in the reference space (Table 2). The validation space consisted of $5 \times 5 \times 3 = 75$ simulations.

2.2 Extraction of Simulated Data

In order to speed up the simulations, all photons emerging at $0.13 \leqslant \rho \leqslant 2.17$ mm were detected. The detection area was divided into concentric rings, the width of which coincided with the diameter of the individual fibers (0.23 mm including core and cladding, or 0.2 mm excluding the cladding). However, since the differential area of each ring at a certain radial distance from the source will not automatically match that of a circular fiber at the same ρ, a conversion algorithm was devised in order to adjust the number of detected photons (Appendix A and B). The simulation data was imported into MATLAB® 6.0, and processed to yield a light intensity decay, representative of the geometrical and optical properties of the simulation model, as described in Appendix B.

2.3 Estimation of Photon Pathlength: Preprocessing

The average pathlength migrated by the photons was predicted either with or without data preprocessing. Two basic preprocessing methods were employed.

2.3.1 *Linearization and Data Fitting to an Analytic Expression*

For each combination of optical properties, the simulated intensity decay (Appendix B) was fitted to the following expression of the spatially resolved diffuse reflectance $[R_i = R(\rho_i)]$ as a function of the discrete source detector separation, ρ_i ($\rho_i = 0.23, 0.46, \ldots, 2.07$ mm):

$$\ln R_i = m_1 - m_2 \ln \rho_i - m_3 \rho_i, \tag{3}$$

where $m_1 = \ln m_1'$. This is the logarithmic form of a modified expression originating from diffusion theory, introduced by Groenhuis et al.[5] This form of the expression was introduced in order to minimize the relative fitting error in a least squares sense, using linear regression, solving for m_1, m_2, and m_3. None of the three parameters m_1, m_2, or m_3 were fixed, and the number of fibers used for the fitting of the above expression was varied. In contrast, some authors[5–7] have used set values of m_2 (0.5, 1, and 2), whereas others have not.[3] From the earlier expression, it is evident that m_1 acts as an amplification factor, and is thus dependent on absolute measurements of the R_i, whereas m_2 and m_3 merely describe the shape of the intensity decay, and not the absolute level.

2.3.2 *Autoscaling*

Two of the interpolation methods discussed in the next section, the *K*-nearest-neighbor method and the linear interpolation using a Delaunay triangulation, will both yield results that depend on the geometrical distances between the predictor data points (in this case m_k and $\ln R_i$). Since the various data sets of predictors (m_k and $\ln R_i$), displayed great numerical differences and variability, an autoscaling approach was applied. All predictors were autoscaled by normalization with the standard deviation (SD) of the predictors calculated from the reference space.[23]

2.4 Estimation of Photon Pathlength: Key Methods

The pathlength, $pl_i = pl(\rho_i)$, is in this context defined as the average of the distances migrated by the photons from point of entry (source fiber) to point of detection (ith detector fiber) (Figure 1). The predicted pathlength, denoted $\widehat{pl}_i$, was derived by using four different estimation methods. The simplest approach in finding $\widehat{pl}_i$, is to determine the mean pl for each source detector separation, ρ_i, as an average of all simulations in the reference data set; thus, devising a method that is only dependent on the source detector separation to predict the pl_i.

The more advanced methods are based on two- or three-dimensional pathlength predictors, consisting of either $\ln R_i$ or m_k values. The *K*-nearest-neighbor (KNN) method estimates pl_i as a weighted sum of the pathlengths corresponding to the *K* closest reference points:

$$\widehat{pl}_i = \sum_{q=1}^{K} \frac{pl_q}{d_q} \Big/ \sum_{q=1}^{K} \frac{1}{d_q}, \tag{4}$$

where d_q denotes the geometrical distance between the point of prediction and the qth closest point in the reference simulation set. Further, a linear interpolation method (LIP) using a Delaunay triangulation of the reference data space, was evaluated (griddata3 in MATLAB® 6.0). Finally, a multiple polynomial regression model of the third degree as a function of m_1, m_2, and m_3 was utilized to estimate pl_i (MPR):

$$\widehat{pl}_i = \widehat{pl}_i(m_1, m_2, m_3) = \sum_{j,k,l} a_{ijkl} m_1^j m_2^k m_3^l, j + k + l \leqslant 3, \tag{5}$$

hence,

$$\widehat{pl}_i = a_{i000} + a_{i100} m_1 + a_{i010} m_2 + a_{i001} m_3 + \ldots + a_{i300} m_1^3 + a_{i030} m_2^3 + a_{i003} m_3^3. \tag{6}$$

The general MPR includes 20 unknown coefficients a_{ijkl} for each of the nine fibers. Model selection, i.e., which of the unknown coefficients that are useful for explaining pl_i was undertaken in STATISTICA™ 5.5, using forward linear regression. The model was then implemented in MATLAB® 6.0. The general model resulted in a nearly singular matrix when determining the coefficients. Therefore, the m_1^3, m_2^3, m_3^3 terms were excluded. All four estimation methods were evaluated by calculating the mean and SD of the ratio between estimated and simulated pathlength ($\widehat{pl}_i/pl_i$), as well as the rms of the relative error $[(\widehat{pl}_i - pl_i)/pl_i]$, for the validation space.

2.5 Estimation of Tissue Perfusion Using the Laser Doppler Principle

Each time a photon interacted with a moving scatterer, the corresponding Doppler shift was recorded. If multiple interactions with moving scatterers occurred, the individual Doppler shifts were summed up. The distribution of Doppler frequency shifts was characterized by calculating a histogram with 24.4 Hz wide frequency bins, centered around 0 Hz. Thereafter, the histogram was convolved with itself, creating a Power spectrum for each detector i, $P_i(\omega)$. Subsequently, the power at negative frequencies were mirrored to the corresponding positive frequencies, and the perfusion estimate, $Perf_i$, was calculated by summation of $\omega P_i(\omega)$, for ω in the interval corresponding to 12–12 500 Hz. Finally, the perfusion estimate was normalized by R_i^2:[13,15]

$$Perf_i = \frac{\Sigma_\omega \omega P_i(\omega)}{R_i^2}. \tag{7}$$

3 Results

The variations in the average photon pathlength as a function of the source detector separation at discrete distances, ρ_i, for the 144 different combinations of optical properties in the reference space is depicted in Figure 2. The mean and SD of the pl_i basically increase linearly with the source detector separation. For the ninth detector fiber ($\rho_i = 2.07$ mm), the

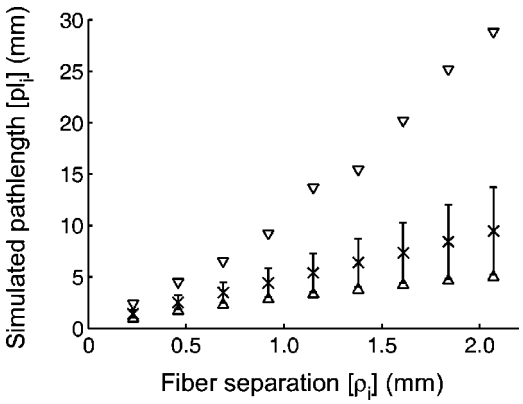

Fig. 2 Variations of pathlength (pl_i) as a function of source detector separation (ρ_i). Mean (x) ± one SD (error bars) are given for each fiber. The triangles denote the maximum and minimum values.

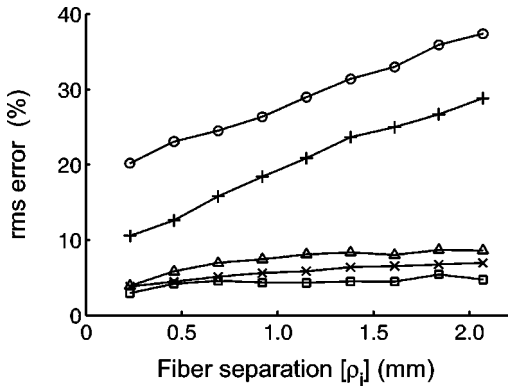

Fig. 4 Prediction of pathlength based on all of the various methods presented in this paper, given as the rms of the relative error [($\widehat{pl}_i - pl_i$)/pl_i] for each method vs ρ_i. Predictions based on: ○, average pathlength, +, KNN method using m_2 and m_3 values based on all nine fibers, △, KNN method using R_i values from fibers 3 and 7, ×, KNN method using m_1, m_2, and m_3 values based on all nine fibers, and □, MPR method using m_1, m_2, and m_3 values based on all nine fibers.

average pl_i varies almost sixfold (5.0–28.8 mm). Even for the first detector fiber ($\rho_i = 0.23$ mm), the ratio between the longest and the shortest pl_i is close to 2.6 (range 0.94–2.41 mm).

The result of predicting pl_i of the validation space using the average pl_i from the reference space is presented in Figures 3 and 4. This method overestimates pl_i by 9%–19% (mean) with a SD of 18%–32%, and a rms of the relative error [($\widehat{pl}_i - pl_i$)/pl_i] of 20%–37% (hereafter referred to as rms error). The range of *pl* ratios ($\widehat{pl}_i/pl_i$) for the ninth fiber was 0.52–1.81.

The more sophisticated prediction methods KNN, LIP, and MPR yielded results with comparable accuracy. However, the LIP method was not able to predict all pl_i, due to the fact that some predictor points in the validation space fell outside the convex hull of the triangulated reference space. Therefore, this method was not further used. As for the KNN method, the data set was preprocessed using autoscaling, since this in general improved accuracy. The KNN method was evaluated for K in the range 1–16 and the optimal K value was chosen individually for each fiber (range 3–10), where the optimal K is defined as the K value resulting in the prediction with the smallest rms error.

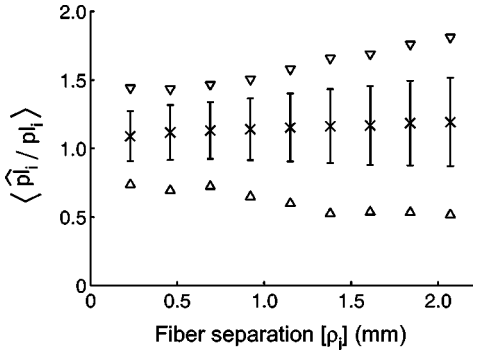

Fig. 3 Prediction of pathlength based on average pathlength. Predicted divided by simulated pathlength ($\widehat{pl}_i/pl_i$) is plotted as a function of source detector separation (ρ_i). Mean (x) ± one SD (error bars) are given for each fiber. The triangles denote the maximum and minimum values.

One previously suggested method,[24] is to predict pl_i based on two R_i values. The R_i from fibers 3 and 7 ($\rho_i = 0.69$ mm and $\rho_i = 1.61$ mm) gave the most accurate $\widehat{pl}_i$ (Figure 4), when applying the KNN method. On average, this method yielded a 1.6%–5.6% overestimation of $\widehat{pl}_i$, with a SD of 3.6%–6.9% and a rms error of 3.9%–8.7%. The range of *pl* ratios for the worst case, fiber nine, was 0.91–1.36.

Extending the KNN approach to three different R_i yielded slightly more accurate and precise results, compared to the case with two different R_i. The R_i values from fibers 2, 4, and 7 appeared to give the most accurate $\widehat{pl}_i$. The $\widehat{pl}_i$ is overestimated by 1.5%–4.5%, with a SD of 4.0%–6.4% and a rms error of 4.2%–7.6%. The range of *pl* ratios for fiber 6 (worst case) is 0.83–1.24. For the sake of clarity, these data were excluded from Figure 4.

Estimation of pl_i based on m_2 and m_3 (derived from all nine fibers) using the KNN method is also presented in Figure 4. The $\widehat{pl}_i$ is overestimated by 2.4%–7.3%, with a SD of 10.3%–28.1% and a rms error of 10.5%–28.8%. The worst case range of *pl* ratios was for fiber 9 (0.41–2.01).

The KNN method using m_1, m_2, and m_3, predicted pl_i to within −0.09%–1.1%, with a SD of 3.8%–6.9% and a rms error of 3.8%–7.0% (Figure 4). The worst case range of *pl* ratios (fiber 9) was between 0.82 and 1.16. Decreasing the number of detectors in the fitting to Eq. (3) results in a decreased accuracy and precision of the $\widehat{pl}_i$ using the KNN method. In all cases, the best predictions are obtained using all nine detectors. However, generally, accuracy and precision was maintained down to using only the five detector fibers closest to the source. After removal of more fibers, accuracy unequivocally deteriorated.

Applying the MPR method to the same m_1, m_2, and m_3 data set, slightly improved the predictions (Figures 4 and 5). The $\widehat{pl}_i$ mean error ranged between −0.01% and 0.78% of the simulated pl_i using all nine detectors, with a SD of 3.0%–5.5% and a rms error of 3.0%–5.4%. The range of *pl* ratios for fiber 6 (worst case) was 0.86–1.15.

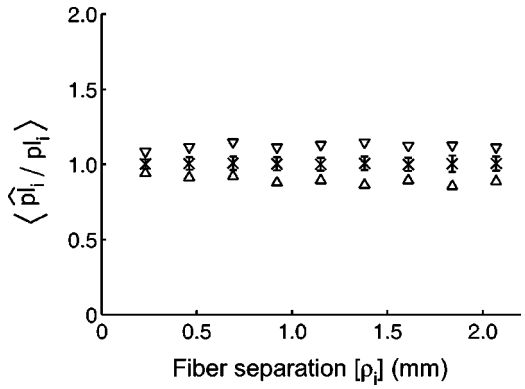

Fig. 5 Prediction of pathlength based on calculated m_1, m_2, and m_3 values using the MPR method and all nine fibers in the data fitting to Eq. (3). Predicted divided by simulated pathlength is plotted as a function of ρ_i. Mean (x) ± one SD (error bars) are given for each fiber. The triangles denote the maximum and minimum values.

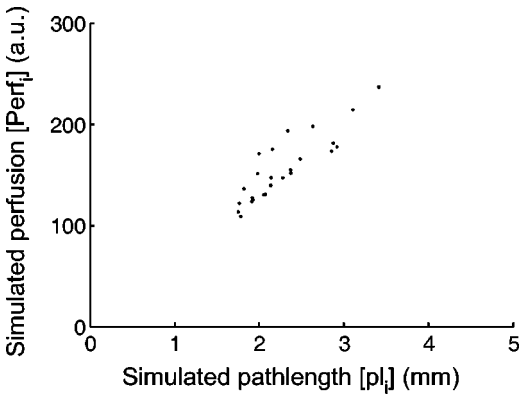

Fig. 7 Perfusion estimates vs pl_i for $\rho_i = 0.46$ mm and $\langle \cos\theta \rangle = 0.875$. The span of optical properties is defined in Table 2.

For a fixed $\langle \cos\theta \rangle = 0.875$, the calculated LDF perfusion [Eq. (7)] increases almost linearly with pl_i (Figure 6). The perfusion estimate ranges from 69–694 a.u., considering all source detector separations. Even within one fiber, the perfusion estimate can vary substantially. At $\rho_i = 0.46$ mm, the perfusion estimate varies between 109 and 237 a.u. (Figure 7), and increases linearly with pl_i (ranging from 1.75 to 3.41 mm).

4 Discussion

The aim of this study was to devise a method that could estimate the average pathlength, pl_i, migrated by photons in turbid media, at discrete source detector separations, ρ_i. The method has to be robust and applicable to a wide range of optical properties, in order to be useful in a clinical setting. It should be easy to measure and calculate the predictors, allowing the investigator to monitor pathlength variations *in vivo*, preferably real time. The tissue volumetric resolution of the optical properties and, hence, pathlength determination, depends on the source detector separation, ρ. Using a small ρ, local tissue inhomogeneities in the mm^3 range can be revealed.[2] By using a larger ρ, the influence of deeper tissue structures in the cm^3 domain is detected.[10] We present a method, based on the spatially resolved diffuse reflectance in the 0–2 mm range, that yields $\widehat{pl}_i$ with a rms error of approximately 5%.

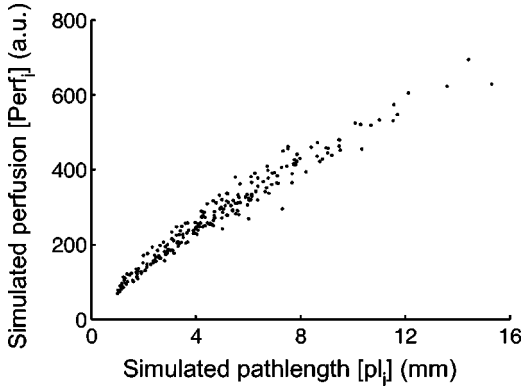

Fig. 6 Perfusion estimates ($Perf_i$) as a function of average pathlength, depicted for all ρ_i and $\langle \cos\theta \rangle = 0.875$. The span of optical properties is defined in Table 2.

The significance of being able to predict *pl* is illustrated in Figure 2. The longest pathlength migrated by a photon can be almost six times greater than the shortest one with a source detector separation of 2.07 mm. Source detector separations up to about one mm can yield more than three-fold variations in *pl* (2.8–9.2 mm).

A number of different methods for predicting the pl_i are presented in this paper. All but one are based on measuring the diffuse reflectance, at two to nine discrete detector locations. The simplest method finds $\widehat{pl}_i$ based on the average of the simulated photon pathlengths as a function of ρ_i; thus, rendering any measurements unnecessary. However, these predictions have a systematic overestimation of 9%–19% and large SDs, probably due to the choice of validation data set, making this method less useful.

Of the three remaining estimation methods evaluated in this study, only one is independent of the absolute magnitude of the diffuse reflectance, R_i, thereby avoiding problems with absolute intensity calibration. This method uses a combined preprocessing technique of linearization and data fitting to an analytic expression, originating from diffusion theory [Eq. (3)], and results in two parameters (m_2 and m_3) that merely describe the shape of R_i vs ρ_i, but not the absolute magnitude. Obviously, information is lost this way, but estimations are still more accurate than the previous method in predicting pl_i. However, the method is far too imprecise, with rms errors up to 29%. This result is in agreement with those of Dam et al. who found that predicting optical properties based on relative reflectance profiles was 5–10 times less accurate than using absolute reflectance.[3]

One intuitive approach previously suggested by us, is using the diffuse reflectance detected in two (neighboring) fibers as predictors.[24] The choice of fibers will strongly influence the accuracy of the prediction algorithm. We found slight overestimations of pl_i of up to 5.6%, and rms errors up to 8.7%. Obviously, the method can be expanded to incorporate more than two fibers in the analysis. The case of three different fibers improved results slightly, with overestimations ranging up to 4.5%. A major drawback with this method is the inher-

ent sensitivity to disturbances in any one of the channels/fibers during measurement.[4]

In order to condense the information from measurements, and to reduce sensitivity to data collection disturbance in one or several fibers, it is practical to fit diffuse reflectance data to an analytic expression [Eq. (3)], as mentioned previously. Using all three parameters, m_1, m_2, and m_3, in describing the R_i, both the shape (m_2 and m_3) and absolute magnitude (m_1) are considered. The best accuracy in predicting pl_i based on m_1, m_2, and m_3 was seen if all nine simulated fibers were used in the data fitting. The KNN method was considered an intuitive approach in finding $\widehat{pl}_i$, but required relatively high K values (3–10) to yield accurate estimates. Better estimates were found using a multiple polynomial regression model of the third degree. This way, $\widehat{pl}_i$ based on m_1, m_2, and m_3 became very accurate (overestimations up to 0.8%) and precise (SD and rms error up to 5.5%). The worst case range of $\widehat{pl}_i/pl_i$ was 0.86–1.15 (fiber 6).

The accuracy and precision should be viewed in light of the choice of optical parameters in the reference and validation space (Tables 1 and 2), where the parameters in the validation space were chosen to maximize the distances to the nearest combinations of optical properties in the reference space. Thus, the accuracy listed earlier for the various prediction methods are expected to be the worst case scenarios.

All the aforementioned results are based on a fixed relation between the isotropic and the anisotropic component of the phase function, but with varying $\langle \cos\theta \rangle$. The importance of the phase function in determining the reflectance profile, depends on the source detector separation, expressed in terms of $\rho\mu_s'$.[2] For a high albedo and $\rho\mu_s' > 10$, the diffusion approximation holds and the reflectance only depends on μ_a and μ_s'. The diffusion approximation can be extended to smaller distances, but only if the phase function is known.[2] Generally, for separations in the range $0.5 < \rho\mu_s' < 10$, the reflectance depends on the first and second moment of the phase function and for smaller distances on even higher moments of the phase function.[2] In our study, the range of optical properties is wide in the sense that source-detector separations of 2 mm yield $\rho\mu_s'$ in the range 0.5–20. Since our model almost encompasses all three regimes mentioned earlier, Monte Carlo simulations were chosen to determine the reflectance. One limitation of this study is, that we did not consider other combinations of phase functions. To do this, however, the range of optical properties should be divided into smaller sets corresponding to the $\rho\mu_s'$ regimes mentioned earlier.

It has been proposed that μ_a and μ_s' should be measured in the diffusive region and the phase function at small distances.[1,2] This and other studies have shown that limiting the separation reduces the estimation accuracy.[25] Therefore, there is a trade off between spatial resolution and the estimation accuracy. Our results were obtained with a single layer model. To predict the optical properties and, hence, the photon pathlength for a layered model, requires some *a priori* knowledge of the layer structure and the optical properties of the layers.[6,26]

From Figure 6, the need for correction of pathlength-related variations in the LDF perfusion estimate is obvious. While the true perfusion through the slab is kept constant, and the optical properties are varied according to Table 2 (fixed $\langle \cos\theta \rangle = 0.875$), the estimated perfusion value displays a tenfold difference between its lowest and highest value, looking at all source detector separations. Hence, at least part of an increase in the LDF perfusion signal with increasing ρ_i, traditionally attributed to sampling deeper more highly perfused areas, could simply be related to a longer pl_i, and, thus, greater probability of interaction with moving scatterers. Further, it is logical to assume that the probability of multiple Doppler shifts and nonlinear homodyne effects increase with longer pathlengths. Thus, the slope of the perfusion is expected to be somewhat underestimated for increasing pl_i.[27] In a fixed fiber, at a distance relevant to LDF ($\rho_i = 0.46$ mm), the perfusion estimate varied between 109 and 237 a.u. (Figure 7), and increased linearly with pl_i (ranging from 1.75 to 3.41 mm). It is evident that a compensation for this pathlength-related perfusion variation could improve LDF accuracy.

5 Conclusion

In this study, we have demonstrated the substantial variations in pathlength traversed by individual photons through a turbid medium, with optical properties relevant to human skin. We present a multiple polynomial regression method that, based on spatially resolved diffuse reflectance, can predict the average pathlength as a function of source detector separation (up to 2 mm) with a rms error of about 5%. The *K*-nearest neighbor method was the other key approach investigated. It yielded slightly less precise predictions with a rms error of approximately 7%. If no preprocessing was carried out on the reflectance data, the accuracy deteriorated, but the precision was essentially retained. Finally, the average pathlength as a function of source detector separation was also predicted based on the average of all simulated photon paths, yielding gross overestimations and a rms error of up to almost 40%. The results implicate that LDF perfusion estimates can be improved by assessing the pathlength. Other possible applications are reflectance spectroscopy and pulse oximetry.

Acknowledgments

This study was supported by the European Commission through the SMT4-CT97-2148 contract. Under this contract, a cooperation runs between the Universities of Twente and Groningen (the Netherlands), Linköping and Malmö (Sweden), Toulouse (France), the companies Perimed AB (Sweden), Moor Instruments and Oxford Optronix (UK), and the Institute of Biocybernetics and Biomedical Engineering in Warsaw (Poland). Financial support was also received from the Swedish Heart Lung Foundation, Project No. 200141208 and MedComp AB, Sweden.

Appendix A

$$\rho^2 = (\rho_i + r\cos\alpha)^2 + (r\sin\alpha)^2 \Rightarrow \cos\alpha = \frac{\rho^2 - \rho_i^2 - r^2}{2\rho_i r};$$

$$\alpha \in [0, \pi],$$

$$\theta = \cos^{-1}\left(\frac{\rho_i + r\cos\alpha}{\rho}\right) = \cos^{-1}\left(\frac{\rho_i^2 + \rho^2 - r^2}{2\rho_i\rho}\right),$$

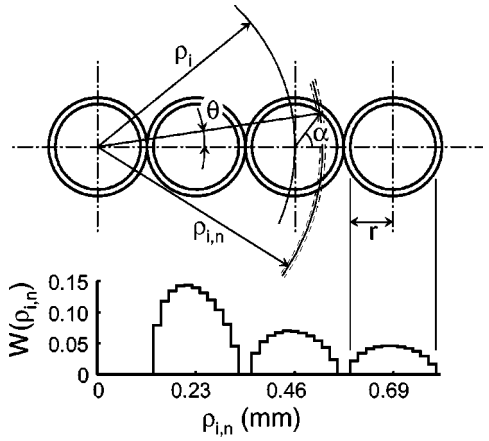

Fig. 8 (Appendix A) Top: Detail of probe design, with four adjacent fibers, including cladding. ρ_i = distance from center of source fiber to center of *i*th detector fiber, $\rho_{i,n}$ = distance from center of source fiber to center of nth subpartition in *i*th detector fiber, ρ = radial distance from center of source fiber to arbitrary point in the *i*th detector fiber, r = core radius of fiber. Bottom: Ring-to-fiber weighting factor, $W(\rho_{i,n})$, as a function of the distance to the center of the source fiber.

$$dA_c = 2\theta\rho d\rho,$$

$$dA_r = 2\pi\rho d\rho,$$

$\therefore$ the weighting factor, $W(\rho)$, (see Figure 8) for every ρ, $\rho_i - r \leq \rho \leq \rho_i + r$, is

$$W(\rho) = \frac{dA_c}{dA_r} = \frac{1}{\pi}\cos^{-1}\left(\frac{\rho_i^2 + \rho^2 - r^2}{2\rho_i\rho}\right).$$

Appendix B

1. The *i*th ring, representing the *i*th fiber, was subdivided into N_s subpartitions ($N_s = 11$ was deemed most adequate considering speed of computation and accuracy), and the number of photons detected within the *n*th subpartition, $I_r(\rho_{i,n})$, was determined.
2. $W(\rho_{i,n})$ was calculated for all subpartitions, and the normalized weighting factor, $NW(\rho_{i,n}) = W(\rho_{i,n})/\max W(\rho_i)$ was determined.
3. A number of photons from each subpartition, equaling $NW(\rho_{i,n})I_r(\rho_{i,n})$, was randomly picked from the total number of detected photons within each subpartition. These photons were subsequently used to calculate mean pathlength and Doppler frequencies.
4. Finally, $R_i = \Sigma_{n=1}^{N_s} W(\rho_{i,n})I_r(\rho_{i,n})/N_{\text{emitted}}$, where N_{emitted} = number of emitted photons.

References

1. F. Bevilacqua, D. Piguet, P. Marquet, J. D. Gross, B. J. Tromberg, and C. Depeursinge, ''*In vivo* local determination of tissue optical properties: Applications to human brain,'' *Appl. Opt.* **38**(22), 4939–4950 (1999).
2. F. Bevilacqua and C. Depeursinge, ''Monte carlo study of diffuse reflectance at source-detector separations close to one transport mean free path,'' *J. Opt. Soc. Am. A* **16**(12), 2935–2945 (1999).
3. J. S. Dam, P. E. Andersen, T. Dalgaard, and P. E. Fabricius, ''Determination of tissue optical properties from diffuse reflectance profiles by multivariate calibration,'' *Appl. Opt.* **37**(4), 772–778 (1998).
4. J. S. Dam, C. B. Pedersen, T. Dalgaard, P. E. Fabricius, A. Prakasa, and S. Andersson-Engels, ''Fiber optic probe for non-invasive real-time determination of tissue optical properties at multiple wavelengths,'' *Appl. Opt.* **40**(7), 1155–1164 (2001).
5. R. A. J. Groenhuis, J. J. Ten Bosch, and H. A. Ferwerda, ''Scattering and absorption of turbid materials determined from reflection measurements. 2: Measuring method and calibration,'' *Appl. Opt.* **22**(16), 2463–2467 (1983).
6. J. M. Schmitt, G. X. Zhou, E. C. Walker, and R. T. Wall, ''Multilayer model of photon diffusion in skin,'' *J. Opt. Soc. Am. A* **7**(11), 2141–2153 (1990).
7. B. C. Wilson and S. L. Jacques, ''Optical reflectance and transmission of tissues: Principles and applications,'' *IEEE J. Quantum Electron.* **26**, 2186–2199 (1990).
8. A. Kienle, L. Lilge, M. S. Patterson, R. Hibst, R. Steiner, and B. C. Wilson, ''Spatially resolved absolute diffuse reflectance measurements for noninvasive determination of the optical scattering and absorption coefficients of biological tissue,'' *Appl. Opt.* **35**(13), 2304–2314 (1996).
9. J. R. Mourant, T. Fuselier, J. Boyer, T. M. Johnson, and I. J. Bigio, ''Predictions and measurements of scattering and absorption over broad wavelength ranges in tissue phantoms,'' *Appl. Opt.* **36**(4), 949–957 (1997).
10. B. J. Tromberg, N. Shah, R. Lanning, A. Cerussi, J. Espinoza, T. Pham, L. Svaasand, and J. Butler, ''Noninvasive *in vivo* characterization of breast tumors using photon migration spectroscopy,'' *Neoplasia* **2**(1–2), 26–40 (2000).
11. W.-F. Cheong, ''Summary of optical properties,'' in *Optical-Thermal Response of Laser-Irradiated Tissue*, A. J. Welch and M. J. C. van Gemert, Eds., pp. 275–303, Plenum, New York (1995).
12. M. Larsson, W. Steenbergen, and T. Strömberg, ''Influence of optical properties and fibre separation on laser doppler flowmetry,'' *J. Biomed. Opt.* **7**(2), 236–243 (2002).
13. G. E. Nilsson, ''Signal processor for laser doppler tissue flowmeters,'' *Med. Biol. Eng. Comput.* **22**, 343–348 (1984).
14. R. F. Bonner and R. Nossal, ''2. Principles of laser-doppler flowmetry,'' in *Laser-Doppler Blood Flowmetry*, A. P. Shepherd and P. Å. Öberg, Eds., pp. 17–45, Kluwer Academic, Boston (1990).
15. R. Nossal, R. F. Bonner, and G. H. Weiss, ''Influence of path length on remote optical sensing of properties of biological tissue,'' *Appl. Opt.* **28**(12), 2238–2244 (1989).
16. S. T. Flock, M. S. Patterson, B. C. Wilson, and D. R. Wyman, ''Monte carlo modeling of light propagation in highly scattering tissues—I: Model predictions and comparison with diffusion theory,'' *IEEE Trans. Biomed. Eng.* **36**(12), 1162–1168 (1989).
17. A. M. K. Enejder, ''Light scattering and absorption in tissue—models and measurements,'' PhD thesis, Department of Physics, Lund Institute of Technology, Lund University, Lund, 1997.
18. F. F. M. de Mul, M. H. Koelink, M. L. Kok, P. J. Harmsma, J. Greve, R. Graaff, and J. G. Aarnoudse, ''Laser doppler velocimetry and monte carlo simulations on models for blood perfusion in tissue,'' *Appl. Opt.* **34**(28), 6595–6611 (1995).
19. M. J. C. van Gemert, S. L. Jacques, H. J. C. M. Sterenborg, and W. M. Star, ''Skin optics,'' *IEEE Trans. Biomed. Eng.* **36**(12), 1146–1154 (1989).
20. V. V. Tuchin, ''Optical properties of tissues with strong (multiple) scattering,'' in *Tissue optics: Light Scattering Methods and Instruments for Medical Diagnosis*, D. C. O'Shea, Ed., pp. 13–33, SPIE, Bellingham, WA (2000).
21. L. G. Henyey and J. L. Greenstein, ''Diffuse radiation in the galaxy,'' *Astrophys. J.* **93**, 70–83 (1941).
22. R. Graaff, A. C. M. Dassel, M. H. Koelink, F. F. M. de Mul, J. G. Aarnoudse, and W. G. Zijlstra, ''Optical properties of human dermis *in vitro* and *in vivo*,'' *Appl. Opt.* **32**(4), 435–447 (1993).
23. J. S. Dam, ''Optical analysis of biological media—continuous wave diffuse spectroscopy,'' PhD thesis, Department of Physics, Lund Institute of Technology, Lund, Sweden, 2000.
24. H. Nilsson and G. Nilsson, ''Light interaction with human cutaneous blood vessels determined by monte carlo simulations—compensation for pathlength dependence in laser doppler flowmetry,'' *J. Vasc. Res.* **35**, 82 (1998).
25. T. H. Pham, F. Bevilacqua, T. Spott, J. S. Dam, B. J. Tromberg, and S. Andersson-Engels, ''Quantifying the absorption and reduced scattering coefficients of tissue-like turbid media over a broad spectral

range using a non-contact Fourier interferometric, hyperspectral imaging system,'' *Appl. Opt.* **39**(34), 6487–6497 (2000).
26. P. E. Andersen, J. S. Dam, P. M. Petersen, and P. Bjerring, ''Local diffuse reflectance from three-layered skin tissue structures, *Optical Tomography and Spectroscopy of Tissue: Theory, Instrumentation, Model, and Human Studies II*,'' *Proc. SPIE* **2979**, 515–526 (1997).
27. R. F. Bonner and R. Nossal, ''Model for laser doppler measurements of blood flow in tissue,'' *Appl. Opt.* **20**(12), 2097–2107 (1981).